A NIRCam-dark galaxy detected with the MIRI/F1000W filter in the MIDIS/JADES Hubble Ultra Deep Field

Pérez-González, P.G.; Rinaldi, P.; Caputi, K.I.; Álvarez-Márquez, J.; Annunziatella, M.; Langeroodi, D.; ... ; Werf, P.P. van der

The Astrophysical Journal Letters, 969:L10 (12pp), 2024 July 1 https://doi.org/10.3847/2041-8213/ad517b

A NIRCam-dark Galaxy Detected with the MIRI/F1000W Filter in the MIDIS/JADES Hubble Ultra Deep Field

Pablo G. Pérez-González[1], Pierluigi Rinaldi[2], Karina I. Caputi[2], Javier Álvarez-Márquez[1], Marianna Annunziatella[1], Danial Langeroodi[3], Thibaud Moutard[4], Leindert Boogaard[5], Edoardo Iani[2], Jens Melinder[6], Luca Costantin[1], Göran Östlin[6], Luis Colina[1], Thomas R. Greve[7,8,9], Gillian Wright[10], Almudena Alonso-Herrero[11], Arjan Bik[6], Sarah E. I. Bosman[12,13], Alejandro Crespo Gómez[1], Daniel Dicken[10], Andreas Eckart[14], Macarena García-Marín[15], Steven Gillman[7,8], Manuel Güdel[16,17], Thomas Henning[5], Jens Hjorth[3], Iris Jermann[7,8], Álvaro Labiano[18], Romain A. Meyer[19], Florian Peißker[14], John P. Pye[20], Thomas P. Ray[21], Tuomo Tikkanen[20], Fabian Walter[5], and Paul P. van der Werf[22]

[1] Centro de Astrobiología (CAB), CSIC-INTA, Ctra. de Ajalvir km 4, Torrejón de Ardoz, E-28850, Madrid, Spain
[2] Kapteyn Astronomical Institute, University of Groningen, P.O. Box 800, 9700 AV Groningen, The Netherlands
[3] DARK, Niels Bohr Institute, University of Copenhagen, Jagtvej 155, 2200 Copenhagen, Denmark
[4] European Space Agency (ESA), European Space Astronomy Centre (ESAC), Camino Bajo del Castillo s/n, 28692 Villanueva de la Cañada, Madrid, Spain
[5] Max Planck Institut für Astronomie, Königstuhl 17, D-69117, Heidelberg, Germany
[6] Department of Astronomy, Stockholm University, Oscar Klein Centre, AlbaNova University Centre, 106 91 Stockholm, Sweden
[7] Cosmic Dawn Center (DAWN), Denmark
[8] DTU Space, Technical University of Denmark, Elektrovej, Building 328, 2800, Kgs. Lyngby, Denmark
[9] Dept. of Physics and Astronomy, University College London, Gower Street, London WC1E 6BT, UK
[10] UK Astronomy Technology Centre, Royal Observatory Edinburgh, Blackford Hill, Edinburgh EH9 3HJ, UK
[11] Centro de Astrobiología (CAB), CSIC-INTA, Camino Bajo del Castillo s/n, E-28692 Villanueva de la Cañada, Madrid, Spain
[12] Institute for Theoretical Physics, Heidelberg University, Philosophenweg 12, D-69120, Heidelberg, Germany
[13] Max-Planck-Institut für Astronomie, Königstuhl 17, 69117 Heidelberg, Germany
[14] I.Physikalisches Institut der Universität zu Köln, Zülpicher Str. 77, 50937 Köln, Germany
[15] European Space Agency, Space Telescope Science Institute, Baltimore, MD 21218, USA
[16] Dept. of Astrophysics, University of Vienna, Türkenschanzstr 17, A-1180 Vienna, Austria
[17] ETH Zürich, Institute for Particle Physics and Astrophysics, Wolfgang-Pauli-Str. 27, 8093 Zürich, Switzerland
[18] Telespazio UK for the European Space Agency, ESAC, Camino Bajo del Castillo s/n, 28692 Villanueva de la Cañada, Spain
[19] Department of Astronomy, University of Geneva, Chemin Pegasi 51, 1290 Versoix, Switzerland
[20] School of Physics & Astronomy, Space Research Centre, Space Park Leicester, University of Leicester, 92 Corporation Road, Leicester LE4 5SP, UK
[21] Dublin Institute for Advanced Studies, 31 Fitzwilliam Place, D02 XF86, Dublin, Ireland
[22] Leiden Observatory, Leiden University, P.O. Box 9513, 2300 RA Leiden, The Netherlands
Received 2024 February 26; revised 2024 May 17; accepted 2024 May 25; published 2024 June 24

Abstract

We report the discovery of Cerberus, an extremely red object detected with the MIRI Deep Imaging Survey (MIDIS) observations in the F1000W filter of the Hubble Ultra Deep Field. The object is detected at signal-to-noise ratio (S/N) ∼ 6, with F1000W ∼ 27 mag, and undetected in the NIRCam data gathered by the JWST Advanced Deep Extragalactic Survey (JADES), fainter than the 30.0–30.5 mag 5σ detection limits in individual bands, as well as in the MIDIS F560W ultradeep data (∼29 mag, 5σ). Analyzing the spectral energy distribution built with low-S/N (<5) measurements in individual optical-to-mid-infrared filters and higher-S/N ($\gtrsim$5) measurements in stacked NIRCam data, we discuss the possible nature of this red NIRCam-dark source using a battery of codes. We discard the possibility of Cerberus being a solar system body based on the <0.″016 proper motion in the 1 yr apart JADES and MIDIS observations. A substellar Galactic nature is deemed unlikely, given that the Cerberus's relatively flat NIRCam-to-NIRCam and very red NIRCam-to-MIRI flux ratios are not consistent with any brown dwarf model. The extragalactic nature of Cerberus offers three possibilities: (1) a $z \sim 0.4$ galaxy with strong emission from polycyclic aromatic hydrocarbons—the very low inferred stellar mass, $M_\star = 10^5$–$10^6\,M_\odot$, makes this possibility highly improbable; (2) a dusty galaxy at $z \sim 4$ with an inferred stellar mass $M_\star \sim 10^8\,M_\odot$; and (3) a galaxy with observational properties similar to those of the reddest little red dots discovered around $z \sim 7$, but Cerberus lying at $z \sim 15$, with the rest-frame optical dominated by emission from a dusty torus or a dusty starburst.

Unified Astronomy Thesaurus concepts: Galaxy formation (595); Galaxy evolution (594); High-redshift galaxies (734); Stellar populations (1622); Broad band photometry (184); Galaxy ages (576); Active galactic nuclei (16); James Webb Space Telescope (2291)

1. Introduction

Building increasingly powerful telescopes operating at redder and redder wavelengths and (unexpectedly) discovering new types of galaxies at higher and higher redshifts is a classical industry now, established nearly 40 yr ago. Indeed, deep optical surveys carried out in the late twentieth century using highly sensitive detectors were found to miss interesting galaxy populations of evolved and dust-rich galaxies at cosmological distances, both types being relatively bright at near-infrared wavelengths and easily detectable by new instruments, even though they were significantly less efficient in detecting photons and were affected by much larger backgrounds. The key for their discovery was large (red) colors (flux density ratios typically larger than an order of magnitude) between a near-infrared and an optical band, i.e., they were extremely red objects (EROs).

The first EROs were reported using new ground-based near-infrared telescopes built nearly 40 yr ago. They were found to be members of cosmologically relevant galaxy populations, comprising a variety of galaxies ranging from high-redshift quasars to very young and dust-rich galaxies, or even "high"-redshift passive galaxies (see, among many, Elston et al. 1988; McCarthy 2004; Graham & Dey 1996; Franx et al. 2003; Pozzetti & Mannucci 2000).

With the development of very sensitive instruments on board space telescopes such as Spitzer, the search was moved to longer wavelengths in the mid-infrared, at first compared with optical data sets (Wilson et al. 2004; Yan et al. 2004).

Remarkably, when the Hubble Space Telescope gathered extremely deep data taken in the near-infrared up to 1.6 μm, with surveys such as CANDELS or the WFC3 Hubble Ultra Deep Field (HUDF; Koekemoer et al. 2011; Grogin et al. 2011; Koekemoer et al. 2013), Spitzer/IRAC data were still shown to detect unique distinctively red objects that were only visible at wavelengths longer than 3 μm, or at least were extremely faint in the near-infrared and optical spectral ranges. These so-called HST-dark galaxies were studied for around a decade, with significant uncertainties about their nature due to the strong sensitivity limitations of our multiwavelength telescopes, even those operating in very different observational windows such as the (sub)millimeter range (see, e.g., Simpson et al. 2014; Franco et al. 2018; Alcalde Pampliega et al. 2019; Wang et al. 2019). JWST has started, from the earliest phases of the mission, to shed light on those HST-dark galaxies, i.e., mid-infrared-bright near-infrared/optically faint sources that now constitute the bulk of the JWST galaxy exploration (Pérez-González et al. 2023a; Nelson et al. 2023; Barrufet et al. 2023; Williams et al. 2024; Gillman et al. 2023).

The ERO astrophysical industry is intimately tied to the discovery of submillimeter galaxies (SMGs; Hughes et al. 1998). Indeed, many EROs are dusty starbursts, which appear in mid- and far-infrared surveys in different flavors and with different names, starting from SMGs (see, e.g., Blain et al. 2002; Chapman et al. 2005) but also (hot) dust-obscured galaxies (DOGs, Dey et al. 2008; Narayanan et al. 2010; hotDOGs, Tsai et al. 2015), extremely red quasars (ERQs; Hamann et al. 2017), or, more descriptive from an observational point of view, (ultra)luminous infrared galaxies (U/LIRGs; Sanders & Sanders 1996; Elbaz et al. 2002; Pérez-González et al. 2005; Le Floc'h et al. 2005; Caputi et al. 2007; Magnelli et al. 2009; Madau & Dickinson 2014).

Last but not least, EROs, especially if selected at the faintest magnitudes and with appropriate bands for the color, overlap with very high redshift galaxy samples selected using the Lyman break technique (Steidel et al. 1996) at higher and higher redshifts (e.g., Bouwens et al. 2011).

Remarkably, with the advent of JWST, both industries, searching for red objects and for those with higher and higher redshifts, have been merged at a profound level, with the possibility of finding double-break (Lyman and Balmer) red galaxies (Labbé et al. 2023b), now known as little red dots (LRDs; Furtak et al. 2023; Übler et al. 2023; Matthee et al. 2024; Barro et al. 2024; Greene et al. 2024; Williams et al. 2024; Killi et al. 2023; Pérez-González et al. 2024; Kokorev et al. 2024), or high-redshift galaxies with very high equivalent width emission lines, first discovered with Spitzer (Smit et al. 2014) and now appearing in many JWST works (Pérez-González et al. 2023a; Rinaldi et al. 2023). Interestingly, some of these sources have been confirmed to present broad emission line components possibly linked to an active galactic nucleus (AGN; Kocevski et al. 2023; Greene et al. 2024).

The interesting subtopics of finding and characterizing dusty galaxies on the one hand, and high-redshift galaxy candidates on the other, have been demonstrated to be very relevant for JWST surveys, which can easily misidentify one type of galaxy with the other (see, e.g., Zavala et al. 2023; Naidu et al. 2022).

The MIRI instrument on board JWST (Rieke et al. 2015; Wright et al. 2023) now offers the possibility to search for red galaxies with longer color baselines, beyond the wavelengths first probed by Spitzer/IRAC and now easily accessible with impressive depths (∼30 mag and beyond) using JWST/NIRCam. Even though MIRI cannot reach NIRCam depths, very deep imaging at 5.6–12.8 μm reaching magnitudes around 27–29 is already available and opens a whole new window for the search for and characterization of high-redshift galaxies (Papovich et al. 2023; Barro et al. 2024; Rinaldi et al. 2023; Pérez-González et al. 2024).

In this Letter, we report the discovery of a MIRI-bright red object appearing in the MIRI Deep Imaging Survey (MIDIS) F1000W imaging of the HUDF (Östlin et al. 2024, in preparation). The source is extremely faint at NIRCam long wavelengths, i.e., it is a NIRCam-dark object lying at the edge of the detection limit (∼30.5 mag) of one of the deepest JWST surveys available to date, the JWST Advanced Deep Extragalactic Survey (JADES; Eisenstein et al. 2023b), having not been cataloged before (Rieke et al. 2023; Eisenstein et al. 2023a). Consequently, our object presents an extremely red color between 4.4 and 10 μm, and, in fact, the source is also red with respect to the bluest MIRI filter, as revealed by the MIDIS F560W imaging.

This letter is organized as follows. Section 2 presents the deep MIRI data used in this letter, as well as ancillary observations taken with NIRCam, the Atacama Large Millimeter/submillimeter Array (ALMA), and the Very Large Telescope (VLT). Section 3 describes our method to detect NIRCam-dark galaxies and the case for a positive detection in the HUDF, the source we call Cerberus. Section 4 presents the spectral energy distribution (SED) of Cerberus and briefly discusses the several possible interpretations, analyzing the implied physical properties for each one of them (more information is given in Appendix). Finally, Section 5 presents a summary of our findings.

Throughout the Letter, we assume a flat cosmology with $\Omega_M = 0.3$, $\Omega_\Lambda = 0.7$, and a Hubble constant $H_0 = 70\ \mathrm{km\ s^{-1}\ Mpc^{-1}}$. We use AB magnitudes (Oke & Gunn 1983). All stellar mass and SFR estimations assume a universal Chabrier (2003) initial mass function (IMF), unless stated otherwise.

2. The MIRI Deep F1000W Survey in the HUDF, and Ancillary Data

2.1. MIRI Data

MIRI data in the F1000W filter were taken as part of the MIDIS (Östlin et al. 2024, in preparation; PID 1283) in 2023

December. The observation consisted of 11 exposures, each with 100 groups, FASTR1 readout, and 10 integrations, for a total on-source exposure time of 30,800 s, centered on the HUDF. The dithering pattern was set to large-size cycling, with the 11 exposures taken in different positions on the sky separated by up to 10″.

The reduction of the MIRI data followed the methodology described in Pérez-González et al. (2024), based on the official JWST pipeline (v1.13.4, jwst_1202.pmap) and offline bespoke procedures. Briefly, a superbackground strategy is used to build background maps for each single image using all the other exposures (since they were taken during the same campaign), which results in a very homogeneous background in terms of level and noise. Quantitatively for the data used in this letter, the standard deviation of the background pixels for each cal.fits file obtained with the standard official pipeline is reduced by a factor of ∼3.5 by using our superbackground method, and the depth in the final mosaic improves by 0.8 mag. We refer the reader to Appendix A in Pérez-González et al. (2024) for more details. Known sources are masked to avoid biasing the determination of the very local background in the superbackground image. Our F1000W final mosaic, reduced with 60 mas pixels, presents an average 5σ depth of 26.8 mag, measured in a 0.″4-radius circular aperture and taking into account noise correlation (linked to the drizzling method used in the mosaicking), and after applying the aperture correction (a 1.3 factor).

We present the MIDIS F1000W data in Figure 1 with an RGB image built in combination with some NIRCam long-wavelength data.

2.2. Ancillary Data

In this subsection, we describe other data sets in the HUDF that we have used to complement the MIRI data.

2.2.1. Other MIRI Data

For this letter, we combined the recently acquired MIDIS F1000W data with the F560W ultradeep observations also carried out by MIDIS in 2022 December. These data will be described in Östlin et al. (2024, in preparation) and consist of ∼40 hr on source taken in the HUDF, which allowed us to reach 28.7 mag 5σ for pointlike sources measured in an $r = 0.''23$ circular aperture (the radius being chosen to ensure a ∼70% encircled energy).

2.2.2. NIRCam Data

The MIRI/F1000W data were also complemented with NIRCam imaging taken by JADES (Eisenstein et al. 2023b), Data Release 2 (Eisenstein et al. 2023a), which includes observations from the JWST Extragalactic Medium-band Survey (JEMS; Williams et al. 2023) and the First Reionization Epoch Spectroscopically Complete Observations (FRESCO; Oesch et al. 2023). This data set provides a total of 14 bands from 0.9 to 4.8 μm (6 at short wavelength, SW, and 8 at long wavelength, LW), with 5σ depths ranging from 30.5 to 30.9 mag (measured in 0.″2-radius circular apertures). We remark that JADES is one of the deepest NIRCam surveys on the sky, only matched in depth (in some bands) by the MIDIS NIRCam-parallel project (Pérez-González et al. 2023b) and the Next Generation Deep Extragalactic Exploratory Public Near-Infrared Slitless Survey (NGDEEP; Bagley et al. 2024), which means that our search for NIRCam-dark galaxies is really probing the current depth limitations of JWST extragalactic surveys.

2.2.3. ALMA Data

The ALMA Spectroscopic Survey in the HUDF (ASPECS) is a Cycle 4 Large Program over a 4.6 arcmin^2 scan at 1.2 mm (Decarli et al. 2020; González-López et al. 2020) and 3.0 mm (Decarli et al. 2019; González-López et al. 2019). The ultradeep 1.2 mm data reach an rms sensitivity of 9.3 μJy beam^{-1}, with beam dimensions of $1.''5 \times 1.''1$. The 3.0 mm data reach 1.4 μJy beam^{-1}, with a $1.''8 \times 1.''5$ beam.

2.2.4. MUSE Data

The HUDF has been extensively studied in the past decade with the Multi Unit Spectroscopic Explorer (MUSE; Bacon et al. 2010) mounted on the VLT as part of the MOSAIC and UDF-10 fields (GTO programs 094.A–0289(B), 095.A–0010 (A), 096.A–0045(A), and 096.A–0045(B); PI: R. Bacon) and the most recent MXDF observations (GTO Large Program 1101.A-0127; PI: R. Bacon). The MUSE data have a spectral wavelength range between 4700 and 9300 Å and a spectral resolving power (R) that ranges from 1770 (4800 Å) to 3590 (9300 Å). The HUDF data set was taken during 140 hr on source with the VLT Adaptive Optics Facility (AOF) and its GALACSI adaptive optics module, as detailed in Kolb et al. (2016) and Madec et al. (2018), achieving a spatial sampling of $0.''2 \times 0.''2$, with strong variations of up to a factor of 4. More details about these programs can be found in Bacon et al. (2017, 2023).

3. Selection and Validation of NIRCam-dark Sources

This letter presents a source that was discovered on the MIDIS F1000W image and found not to be included in existing NIRCam published catalogs (Rieke et al. 2023; Eisenstein et al. 2023a). In this section, we describe the selection procedure for such types of NIRCam-dark sources.

3.1. Selection of NIRCam-dark Sources

In order to select NIRCam-dark sources, we executed the SExtractor software (Bertin & Arnouts 1996) directly using the MIRI/F1000W as the detection image. We followed the hot-mode extraction described in Galametz et al. (2013), which is particularly effective for detecting extremely faint sources.

Once we had a hot MIRI/F1000W catalog, we anti-cross-matched it (using a 0.″3 search radius) with the official JADES DR2 catalog published by Eisenstein et al. (2023a, which superseded the DR1 catalog), constructed by selecting sources in an LW stack. The goal of the anti-cross-match was to isolate sources uniquely detected by MIRI/F1000W. The result was a list of 17 *potential* NIRCam-dark sources selected at 10 μm.

We meticulously examined each of the potential NIRCam-dark sources in the final mosaic to rule out the presence of an unflagged cosmic ray or any kind of hot and/or bad pixels that could have caused a spurious detection.

Visual inspection of the individual exposures revealed that for 16 of the 17 candidates there was indeed a hot pixel in one of the 11 exposures that had survived the flagging and stacking process performed to produce the final mosaic. We automated and generalized the source validation methodology by producing

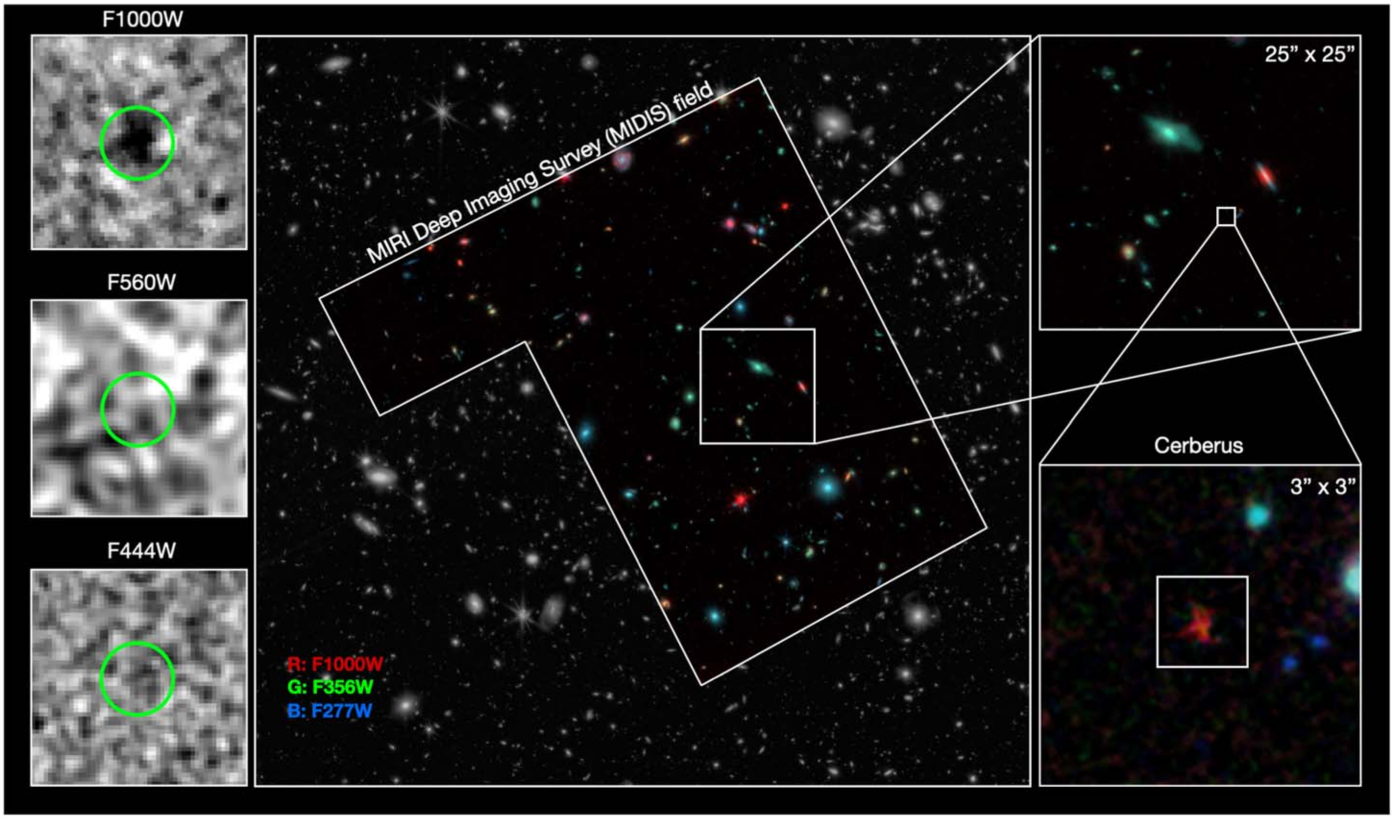

Figure 1. In the center of the figure, we show an RGB composition of the MIDIS F1000W field. The color images have been built with JADES data in two NIRCam filters, F277W and F356W, and the MIDIS MIRI F1000W filter (all images convolved to the same PSF of MIRI/F1000W). In the background, we show the HUDF JADES data in grayscale. We provide a series of zoomed-in RGB frames that lead to the NIRCam-dark MIRI source, Cerberus, whose image is located in the lower right corner. The NIRCam-dark MIRI source Cerberus is highlighted with a square in that RGB frame. Additionally, we provide postage stamp images ($2'' \times 2''$) of Cerberus in MIRI/F1000W, MIRI/F560W, and NIRCam/F444W (left column), showcasing that Cerberus (marked with an $r = 0\farcs25$ green circle) is clearly detected only at 10 μm.

stacked mosaics with a limited number of exposures, excluding one, two, or three of the full set randomly. This procedure, obviously, affects the depth. Explaining the latter case in more detail as an example, we started from our collection of 11 `*_cal.fits` files, and we created the 165 unique mosaics that can be obtained by excluding sets of 3 `*_cal.fits` files for each partial mosaic. After building the 165 realizations, we inspected the 17 potential NIRCam-dark sources, concluding that only one source consistently appeared in all 165 different partial mosaics. The remaining candidates were found to vanish in some of the realizations, in fact even in the mosaics built excluding one single exposure, indicating their most likely spurious nature. To further validate these findings, we made an in-depth analysis of each `*_cal.fits` file, confirming the presence of unflagged hot and/or bad pixels in some of them that indeed led to false detections in a number of the realizations.

One source of the 17 preselected candidates did not vanish in any of the partial mosaics, even when removing three random images. For this source, we measured photometry in a small $0\farcs25$-radius aperture (which maximized signal-to-noise ratio (S/N) on the partial mosaics), as well as the sky noise in a surrounding square $3'' \times 3''$ region, on all the mosaics produced by excluding one, two, and three exposures. We found consistent photometry and a degradation of the S/N consistent with the differences in exposure time. For example, for the skip-3 mosaics, we found an average magnitude of 27.05 ± 0.19 mag, consistent with our measurement in the full mosaic (see Section 4).

However, we found two contiguous exposures, numbers 7 and 8, which, if removed, produced a dimming of the source to 27.4 mag, still within 2σ of the measurement using the full data set. Each one of these exposures has an integration time of 2800 s, with the start of the first exposure and the end of the second separated by $\sim$5700 s. We examined these exposures in detail and found no signs of a cosmic-ray hit but a slightly enhanced signal in an extended region. This could be due to the general properties of the detector (which consistently showed a dimmer region in the superbackground frames for all images). It could also be due to a cosmic-ray shower, which are known to affect MIRI imaging observations (Dicken et al. 2024), with an incidence of several per exposure. Cosmic-ray showers are extended persistence artifacts from cosmic-ray hits and typically affect the detector for several minutes (Wright et al. 2023). However, a high-flux cosmic-ray hit could cause a shower lasting long enough to enhance the signal seen in these exposures. We also note that the enhancement in signal is stronger in exposure 7 compared to exposure 8, which is also consistent with persistence (see Álvarez-Márquez et al. 2023). Given that the two relatively (and slightly) brighter images were contiguous, we do not rule out a transient behavior of the source. Based on the perseverance of the signal from the source in all partial stacks of the MIRI F1000W data set, we concluded that it was not spurious.

The NIRCam-dark source we identified with this methodology was dubbed Cerberus, to acknowledge that it is a weird beast lurking in the darkest corners of the JWST surveys and

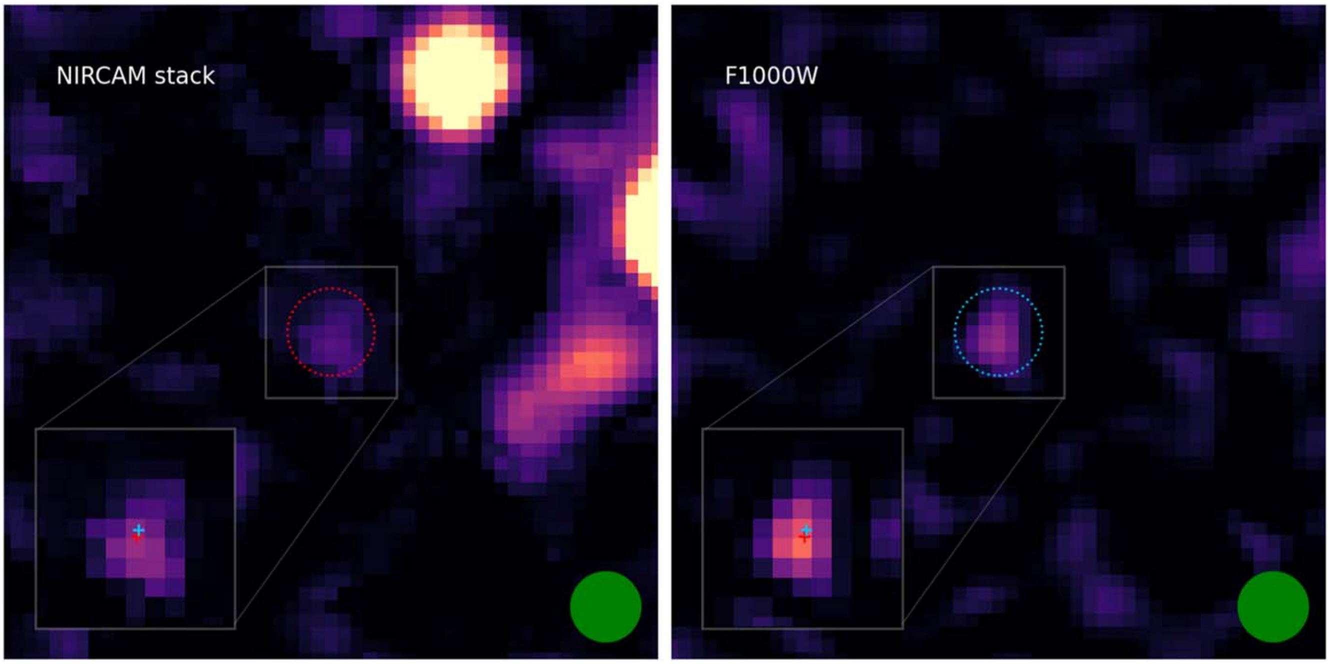

Figure 2. Stacked NIRCam (left panel) and MIRI/F1000W (right panel) images of the region around Cerberus. The stacked NIRCam image was produced from individually PSF-matched LW images. Note that the spurious pixels in the F460M image (see text for details) are removed in the median-stacking procedure. The angular sizes of the images and zoomed-in inset are 3″ × 3″ and 0.″6 × 0.″6, respectively. The red (blue) circle shows the location of the detected source in the NIRCAM stack (F1000W) and has a radius of 0.″2. The green filled circle shows the resolution of the F1000W image (with a diameter of 0.″328). In the zoomed insets, we also show the centroid positions with the blue and red crosses, corresponding to the F1000W image and the NIRCam stack, respectively.

with different interpretations/heads for its nature, as will be shown in Section 4. Its coordinates (J2000) are $\alpha =$ 03:32:38.09 (hr), $\delta = -27$:47:11.81 (degrees). NIRCam and MIRI images of Cerberus are presented in Figure 1.

3.2. Multiwavelength Validation and Observational Properties of the NIRCam-dark Object Cerberus

In order to further validate and characterize Cerberus, we searched for detections by forcing photometric measurements in the data sets described in Section 2, more specifically in the ultradeep observations (among or even the deepest on the sky) provided by JWST/NIRCam, ALMA, and VLT/MUSE.

3.2.1. JWST/NIRCam Measurements

Directly linked to our selection criteria, the NIRCam-dark Cerberus object was not present in any of the catalogs of the JADES NIRCam survey (Rieke et al. 2023; Eisenstein et al. 2023a). We then proceeded to force photometric measurements in all bands (described in Section 4). Forced photometric measurements in all NIRCam individual bands do not provide any measurement $S/N > 5$.

We then stacked NIRCam images to search for faint emission. We constructed two different sets of stacks. One set consisted of cumulative stacks constructed by averaging NIRCam bands starting from the reddest and from the bluest. Another set consisted of disjoint stacks (to avoid noise spikes in one band affecting the measurements in cumulative stacks), combining two, three, four, and five bands, always starting from the reddest and not repeating them in different stacks of the same set.

Figure 2 shows a stacked NIRCam image (including all filters at $\lambda > 3$ μm) convolved to the resolution of the F1000W data (FWHM = 0.″328). Each calibrated individual NIRCam filter was rebinned to a 0.″06 pixel scale and point-spread function (PSF) matched to F1000W using WebbPSF (v. 1.2.1; Perrin et al. 2014) models and the method described in Melinder et al. (2023) and then median-stacked. We measured the centroid of the source for both JWST instruments (using `photutils` with a circular footprint of 3 pixels in radius), finding an agreement within 0.26 pixels, i.e., 0.″016. Remarkably, the source is slightly extended to the northwest in both images. The morphology of the source is similar for the NIRCam stack and the MIRI F1000W image, with a tadpole-like shape extending to the upper right, confirming a detection of the source with NIRCam stacked data (see next section). We also notice a qualitative resemblance between the structure of Cerberus and the $z = 10.6$ galaxy GN-z11 (Oesch et al. 2016; Tacchella et al. 2023), with a concentrated flux distribution identified with the core of the galaxy and an extended haze component.

3.2.2. MUSE Measurements

We extracted the MUSE 1D spectrum at the coordinates of our target within circular apertures of different sizes (0.″4 and 0.″8 radius) but found no significant spectral feature at the position of the NIRCam-dark candidate. This is also confirmed by the publicly available catalog of detected sources by Bacon et al. (2023).

3.2.3. ALMA Measurements

The source is not detected at 1.2 and 3.0 mm. This finding implies 5σ upper limits on the flux density at 1.2 and 3.0 mm of 47 and 7 μJy, respectively, assuming that it is effectively an unresolved pointlike source.

4. Spectral Energy Distribution Analysis of Cerberus

4.1. Multiwavelength Photometry

An SED for Cerberus was built by measuring photometry in all available NIRCam (including both individual bands and stacks) and MIRI data, forcing measurements at the position determined for Cerberus with the MIRI data. Given the faint and small nature of our source, we measured forced photometry in several circular apertures with radii ranging from 0.″1 to 0.″6. We measured the background in a small square region around Cerberus (3″ on the side) and calculated the noise using nonadjacent pixels (5 pixels apart) to take into account noise correlation, as explained in Pérez-González et al. (2023b), obtaining similar depth results (within 0.2 mag) to those reported in Eisenstein et al. (2023b) for the NIRCam bands. Photometric measurements are provided in Table 1.

None of the measurements in individual NIRCam bands have a $>5\sigma$ significance, which we use as our limit to define a detection in each filter.

Given our magnitude measurement in the F1000W band, 27.13 ± 0.17 mag, obtained with photometry in an aperture of radius 0.″3, which maximizes the S/N, and the $S/N \sim 3$ measurements in individual bands and $S/N > 5$ in stacked data for the reddest LW NIRCam channels, we infer a very red color, $F444W - F1000W = 3.8 \pm 0.4$ mag. Using the reddest disjoint stack with an actual detection (i.e., $S/N > 5$), we obtain a color $[4.497] - [10.0] = 2.8 \pm 0.3$ mag.

These measurements indicate that Cerberus is not robustly detected in any individual NIRCam filter but consistent with being slightly below the 5σ detection limits in some bands, quoted to be around 30–31 mag for the JADES DR2 data (Eisenstein et al. 2023b). We remark that the F460M filter, which provides the brightest magnitude, presents a group of 4 pixels to the north of the position of our source, which we confirmed to be an artifact of the reduction, and it is not seen in any other band (even the ones with deeper limiting magnitudes). We excluded this filter from the rest of the analysis.

We measured photometry in the stacked data in the same apertures used for the individual bands, assigning average aperture corrections for the filters included in each stack. The five LW stacks with the highest number of bands all provide $S/N > 5$ fluxes (the average being $S/N \sim 6$), ranging from 29.9 to 30.8 mag. This means that the (low-S/N) SED is characterized by a red color extending through all the $S/N > 5$ stacks from 2 to 4 μm and beyond, up to 29.9 ± 0.2 mag for the first (reddest) stack (including F480M+F444W), which reaches $\sim$5 μm. For the SW stacks, no significant signal is recovered in any of them. We measure a 5σ upper limit of $\sim$31 mag for the stack adding all SW data. The comparison between SW and LW stacks implies a $\gtrsim$0.6 mag color jump from the $\sim$1–2 μm to the $\sim$3–5 μm ranges.

The SED of Cerberus is, in fact, very similar to the LRDs recently presented and characterized in a number of papers (e.g., Labbé et al. 2023b, 2023a; Matthee et al. 2024; Barro et al. 2024; Williams et al. 2024; Pérez-González et al. 2024; Kokorev et al. 2024), but shifted to longer wavelengths. Based on detections of Cerberus in stacked images, we can infer that the $F277W - F444W > 1$ mag general selection criterion of LRDs and, more specifically, the 3 mag color of the example source 203749 in Pérez-González et al. (2024) compare well, if we multiply the observed wavelengths by a factor of $\sim$2, with $F444W - F1000W \sim 3.5$ mag, or, using the F560W 5σ upper limit, $F560W - F1000W \gtrsim 2$ mag. The flat F150W−F200W color distinctive of LRDs (the largest value allowed by the selection is typically 0.5 mag), i.e., a change in slope at around 0.3–0.4 μm in the rest frame for the typical redshift of LRDs $5 < z < 9$, compares well with the color between 3 and 4 μm for Cerberus, just multiplying again the observed wavelengths by a factor of $\sim$2. We remark that this comparison is based on $S/N > 5$ measurements in stacked data. That rest-frame UV color is indeed consistent with the reddest LRDs in Pérez-González et al. (2024) or the LRD of which a NIRSpec

Table 1
Photometric Measurements for the Cerberus Source

Band Name	CWL	Width	Magnitude
F090W	0.903	0.194	>30.0
F115W	1.151	0.225	>30.4
F150W	1.502	0.318	>30.9
F182M	1.847	0.238	>29.8
F200W	1.991	0.461	>30.0
F210M	2.097	0.205	>30.1
F277W	2.786	0.672	31.16 ± 0.28
F335M	3.364	0.347	30.10 ± 0.35
F356W	3.559	0.787	31.22 ± 0.36
F410M	4.084	0.436	30.39 ± 0.40
F430M	4.282	0.229	>30.2
F444W	4.446	1.024	30.91 ± 0.34
F460M	4.630	0.228	29.69 ± 0.36
F480M	4.818	0.304	29.59 ± 0.34
red_stack_01b	4.497	0.755	29.89 ± 0.20
red_stack_02b	4.465	0.771	30.44 ± 0.34
red_stack_03b	4.386	0.665	30.43 ± 0.29
red_stack_04b	4.150	0.937	30.58 ± 0.24
red_stack_05b	4.068	1.047	30.51 ± 0.17
red_stack_06b	3.883	1.231	30.65 ± 0.23
red_stack_07b	3.791	1.296	30.84 ± 0.19
red_stack_08b	3.602	1.446	30.84 ± 0.18
red_stack_09b	3.520	1.524	30.95 ± 0.24
blue_stack_01	1.049	0.392	>30.5
blue_stack_02	1.279	0.628	>30.7
blue_stack_03	1.438	0.846	>31.2
blue_stack_04	1.640	0.658	>30.7
blue_stack_05	1.703	0.742	>31.4
f2_stack_01	4.497	0.755	29.89 ± 0.20
f2_stack_02	4.155	0.331	>30.1
f2_stack_03	3.514	0.602	30.58 ± 0.19
f2_stack_04	2.596	0.750	>30.4
f2_stack_05	1.943	0.355	>30.5
f2_stack_06	1.380	0.496	>30.9
f3_stack_01	4.465	0.771	30.40 ± 0.36
f3_stack_02	3.667	0.822	30.46 ± 0.18
f3_stack_03	2.367	0.604	>31.0
f3_stack_04	1.536	0.711	>31.2
f4_stack_01	4.386	0.665	30.42 ± 0.33
f4_stack_02	3.154	0.989	31.20 ± 0.37
f4_stack_03	1.719	0.594	>31.1
f5_stack_01	4.150	0.937	30.50 ± 0.32
f5_stack_02	2.467	0.892	>31.5
F560W	5.645	1.000	>29.7
F1000W	9.968	1.795	27.13 ± 0.17

Note. The table provides photometric measurements for Cerberus in all NIRCam individual images from JADES, incremental (named red and blue stacks) and disjoint (adding two, three, four, and five contiguous filters) stacks, and MIRI bands from MIDIS. The central wavelengths and widths are given in μm, and the photometry is given in AB magnitudes, including 5σ upper limits for data points with $S/N < 3$.

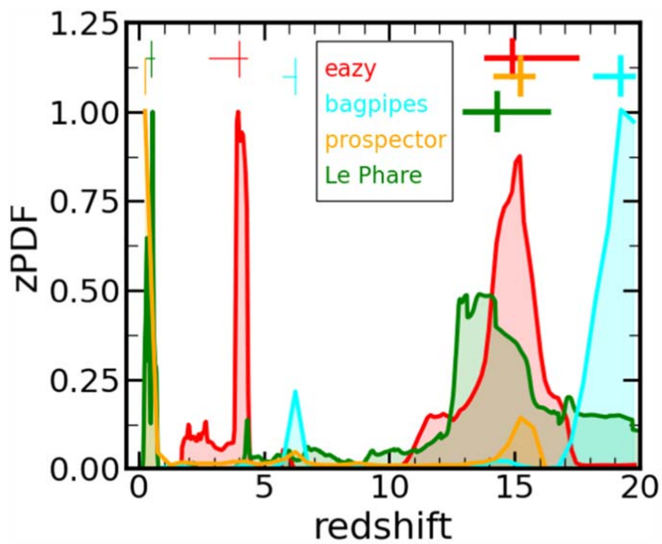

Figure 3. Photometric redshift probability distribution functions of Cerberus. All distributions are normalized to unity at the peak. We show the main solutions and also secondary solutions at $z < 10$ and $z > 10$. Different codes were used in the SED analysis, described in Appendix.

spectrum was presented in Killi et al. (2023). The analogy can also be established in terms of the apparent magnitude: the typical magnitude of LRDs in the blue part of their SED lies around 27–28 mag, Cerberus being $\gtrsim$10 times dimmer in NIRCam LW bands. We note that the difference in luminosity distance between $z \sim 7$, the median redshift of LRDs (Pérez-González et al. 2024), and $z \sim 14$ (a factor of 2 larger; see also Section 4.2.1) will translate to a flux ratio between bands covering the same rest-frame wavelength around an order of magnitude for the same type of object.

4.2. Analysis of the SED of Cerberus

In the following subsections, we discuss possible interpretations of the SED of Cerberus. The NIRCam and MIRI data sets were taken more than 1 yr apart. However, given the spatial coincidence of the object in the NIRCam and MIRI observations (centroids separated by 0$''$016), we proceed by assuming that they are the same object and not a chance alignment of two different objects.

4.2.1. Extragalactic Origin

The SED of Cerberus was fitted to estimate a photometric redshift and obtain its physical properties in a two-step procedure. We used several codes for this purpose, separating the two tasks to analyze facets of each method and understand the (possibly systematic) uncertainties in detail. We used the fluxes described above and the ALMA upper limits quoted in Section 2, shown to be important for high-redshift sources (even for determining their redshift; see Meyer et al. 2024), and particularly for an ERO such as Cerberus. We provide details about the fitting methods in Appendix.

The results of our SED modeling analysis are given in Figure 3 (photometric redshift probability distributions) and Figure 4 (SED models).

We remark that the SED of Cerberus is very noisy, given that it is an ultrafaint source at the very depth edge of the JWST surveys. Therefore, the physical properties of the source are highly uncertain, starting from its redshift (see several peaks in Figure 3).

However, leaving the redshift apart, there are two physical properties for which our results are similar among all SED modeling codes, mainly because they are linked to the two main observational characteristics of Cerberus, i.e., its faintness (translating to relatively low luminosity) and red color. The very red color of our NIRCam-dark object can only be reproduced with significant amounts of dust, linked to either polycyclic aromatic hydrocarbons (PAHs) if the redshift is low, $z \sim 0.4$, or warm/hot dust if the redshift is around $z \sim 4$ or $z \sim 15$. For the lowest redshift, all codes provide very low stellar masses, around $\sim 10^5$–$10^6\,M_\odot$. The combination of very small stellar mass, relatively high dust attenuation, and strong PAH emission is uncommon, at odds with the mass–metallicity relationship (e.g., Tremonti et al. 2004) and the weakening of PAH features at low metallicities (e.g., Engelbracht et al. 2005). For the higher-redshift solutions, $z \sim 4$ and $z \sim 15$, all codes provide masses around $\sim 10^7$–$10^8\,M_\odot$, and they all need large warm dust contents, which can be explained with a very compact starburst or an AGN torus (similar to those detected at high redshift by JWST; see Maiolino et al. 2023; Pacucci et al. 2023; Pacucci & Loeb 2024; Hamann et al. 2017).

4.2.2. Solar System Origin

A bright mid-infrared object such as Cerberus matches the expected properties of solar system bodies, e.g., asteroids. Given the long observational MIRI/F1000W campaign, we would expect to see proper motion, which is not the case, unless the asteroid is distant and/or near aphelion. However, the fact that the NIRCam data detect Cerberus (in stacked images) and the observations from MIDIS and JADES were taken more than 1 yr apart indicates that Cerberus cannot be a solar system body (assuming that the NIRCam and MIRI sources are the same object and not a fortuitous superposition). In Section 3.2, we also measure the centroid shift of the object between the MIRI and NIRCam data to 0$''$016, which is consistent with a zero offset. This makes the source even more unlikely to be a solar system body.

4.2.3. Galactic Origin

As shown by Langeroodi & Hjorth (2023a), Burgasser et al. (2024), and Hainline et al. (2024) for LRDs, red sources detected by JWST in cosmological fields such as GOODS-S or A2744 can be brown dwarfs. Following the method in Langeroodi & Hjorth (2023a), we fit the photometry of Cerberus with brown dwarf atmosphere templates. We include the Sonora cloud-free models (Karalidi et al. 2021; Marley et al. 2021) and the ATMO2020++ cloud-free adiabat-adjusted T and Y dwarf models (Leggett et al. 2021; Meisner et al. 2023; see also Suárez & Metchev 2022). In particular, the ATMO2020++ models were included to ensure coverage of extremely cool brown dwarfs with 250 K $< T_{\rm eff} <$ 500 K. Compared to warmer brown dwarfs, these models more closely resemble the SED shape of Cerberus, which is relatively faint at near-infrared wavelengths while getting significantly brighter at 10 μm.

The best-fit brown dwarf template is shown in the top left panel of Figure 4. We infer a best-fit effective temperature ($T_{\rm eff}$ [K]) of 300^{+100}_{-25}, surface gravity ($\log g$ [cm s^{-2}]) of $3.0^{+1.0}_{-0.5}$, and distance of 332 ± 67 pc. Its effective temperature would most likely classify Cerberus as a Y-type dwarf (see Figure 12 in

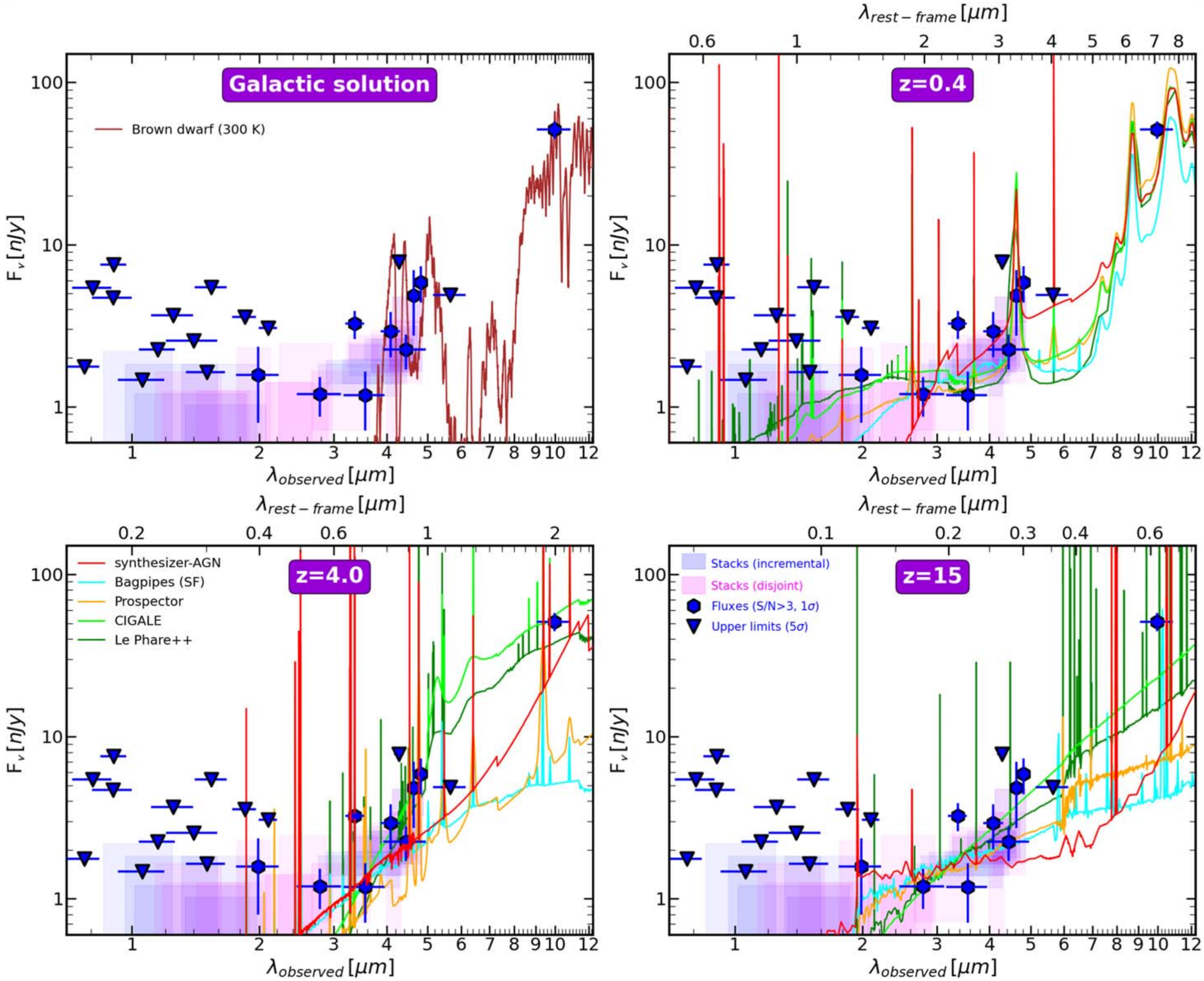

Figure 4. Detailed analysis of the SED of Cerberus for the main redshift solutions. The symbols are the same as described in Figure 3. We provide best-fitting models provided by different codes that include both stellar and AGN emission. The top left panel shows the best-fitting brown dwarf template from the ATMO2020++ models, for a Y-type dwarf with an effective temperature of ∼300 K at a distance of ∼300 pc. The rest of the panels show results for $z = 0.4$ (top right), $z = 3.5$ (bottom left), and $z = 15$ (bottom right).

Langeroodi & Hjorth 2023a). Compared to the UltracoolSheet compilation of known brown dwarfs with parallax distances (Best et al. 2020), its inferred distance (∼300 pc) would make Cerberus one of the farthest (top 20) brown dwarfs discovered to date (see Figure 11 in Langeroodi & Hjorth 2023a). This distance at the high Galactic latitude of Cerberus would place it at the edge of the thin disk (see Figure 6 in Hainline et al. 2024). Recently, three T-type dwarfs were discovered and spectroscopically confirmed with the NIRSpec prism (Langeroodi & Hjorth 2023a; Burgasser et al. 2024) at estimated distances between 0.7 and 4.8 kpc, all most likely outside the thin disk; among them, A2744-BD3 is a late T type at 755 pc.

Our best fit to a brown dwarf spectral template, shown in the top left panel of Figure 4, nicely fits the F444W−F1000W color and is consistent with the nondetection in the deep MIDIS F560W data. However, that brown dwarf model is very red in both the NIRCam SW–LW and 3–4 μm colors, which is not favored by our measurements (in stacked data), pointing to a flatter SED.

In addition, both the MIRI and stacked NIRCam images (see Section 3.2) show the source to be slightly extended and asymmetrical as compared to the PSF. The two instruments, NIRCam and MIRI, indicate a morphology for the source that makes it unlikely that it is a point source, thus disfavoring the *single* brown dwarf scenario.

The slight extension of order $0\farcs1$ alone would not, however, argue against a brown dwarf *binary*. Even at only 100 pc distance, a semimajor axis of $0\farcs1$ for a binary of two identical brown dwarfs/planets with masses of 0.0003–0.07 $M_\odot$ each would result in orbit periods of order 100–1000 yr, i.e., the elongated image would not vary between the NIRCam and the MIRI observations.

5. Summary and Conclusions

We report the discovery of a NIRCam-dark source identified in the MIDIS of the HUDF carried out with the F1000W filter. We call this source Cerberus. The source has a magnitude around 27 mag (6σ) in F1000W and is extremely faint in all the NIRCam data taken by the deepest survey on the sky, JADES, implying a magnitude fainter than $\sim$30.5 at wavelengths $\lesssim 5\,\mu$m. Cerberus is also undetected in the MIDIS F560W ultradeep observations of the field, i.e., F560W $\gtrsim$ 29 mag. Our analysis of MIRI F1000W mosaics produced with limited data sets and the detection in NIRCam stacks at $\sim 5\sigma$ level at wavelengths longer than $\sim 3\,\mu$m both confirm that Cerberus is real and qualifies as an ERO, with a color around F444W–F1000W $\sim$ 3.5 mag and F560W–F1000W $\gtrsim$ 2 mag. The morphology of the source in the MIRI F1000W image matches that observed in the NIRCam stacked data (with 1 yr passing between both observations), in both cases presenting a main pointlike component and similar-sized (i.e., unresolved) haze, further supporting that Cerberus is a real source not linked to a fortuitous alignment.

We discuss the possible nature of Cerberus and identify two possible Galactic source types and three different kinds of galaxy that could match its SED.

Given that the MIRI and NIRCam observations were taken with a 1 yr epoch difference, we discard a solar system origin. The NIRCam-to-NIRCam and NIRCam-to-MIRI colors do not match any known substellar object; even the coolest and reddest brown dwarfs present mid-infrared colors that are not compatible with the SED of Cerberus.

Concerning an extragalactic origin, we identify three possibilities:

1. A low-redshift solution, $z \sim 0.4$, would imply that Cerberus is a dusty galaxy with strong emission from PAHs or warm dust heated by an AGN. The low mass obtained for this solution, $M_\star \sim 10^5\,M_\odot$, would point to an unknown type of dwarf galaxy with large dust content and no PAH depletion.
2. The second possibility is a dusty starburst or post-starburst galaxy, or a galaxy hosting a mid-infrared-bright obscured AGN, at $z \sim 4$ with a stellar mass $M \sim 10^8\,M_\odot$ and high extinction.
3. The third possibility is a $z \sim 15$ galaxy, the red color emanating from an SED dominated by emission from an obscured active nucleus with a bright torus significantly contributing to the flux in the rest-frame optical range, with shorter wavelengths dominated by an $M_\star \sim 10^7\,M_\odot$ galaxy.

Despite vetting all the imaging data meticulously, confirming beyond doubt that the source is real, we have to accept that the available data are insufficient to establish the true nature of Cerberus with certainty. Given that the source is located in the deepest HST and JWST field, deeper imaging will likely be available in the near future and help to obtain a better understanding of this unique object. In any case, further investigation of Cerberus will challenge the capabilities of JWST, as was the case in the past for objects discovered at the limit of photometric surveys (remarkably, with space-based missions such as HST or Spitzer), whose spectroscopic follow-up (typically with ground-based facilities) was tremendously exigent (but still attempted with varying success). The discovery and analysis presented in this letter demonstrate the feasibility of identifying NIRCam-dark sources when selected as EROs with MIRI observations up to at least $10\,\mu$m, maybe revealing new types of Milky Way substellar bodies or of galaxy populations more easily detectable through ultradeep photometric surveys in (some of) the reddest wavelengths probed by JWST.

Acknowledgments

We thank the referee for their constructive comments to our original manuscript. P.G.P.-G. and L.C. acknowledge support from grant PID2022-139567NB-I00 funded by Spanish Ministerio de Ciencia e Innovación MCIN/AEI/10.13039/501100011033, FEDER *Una manera de hacer Europa*. K.I.C. and E.I. acknowledge funding from the Netherlands Research School for Astronomy (NOVA). K.I.C. acknowledges funding from the Dutch Research Council (NWO) through the award of the Vici grant VI.C.212.036. M.A. acknowledges financial support from Comunidad de Madrid under Atracción de Talento grant 2020-T2/TIC-19971. This work was supported by research grants (VIL16599, VIL54489) from VILLUM FONDEN. S.G. acknowledges financial support from the Villum Young Investigator grant 37440 and 13160 and the Cosmic Dawn Center (DAWN), funded by the Danish National Research Foundation (DNRF) under grant No. 140. J.P.P. and T.T. acknowledge financial support from the UK Science and Technology Facilities Council and the UK Space Agency. T.P. R. acknowledges support from ERC Advanced grant 743029 EASY. A.A.H. acknowledges support from grant PID2021-124665NB-I00 funded by the Spanish Ministry of Science and Innovation and the State Agency of Research MCIN/AEI/10.13039/501100011033 and "ERDF A way of making Europe." J.A.-M., A.C.-G., and L.C. acknowledge support by grant PIB2021-127718NB-100 from the Spanish Ministry of Science and Innovation/State Agency of Research MCIN/AEI/10.13039/501100011033 and by "ERDF A way of making Europe." S.E.I.B. is funded by the Deutsche Forschungsgemeinschaft (DFG) under Emmy Noether grant No. BO 5771/1-1. J.M., G.Ö., and A.B. acknowledge support from the Swedish National Space Administration (SNSA). R.A.M. acknowledges support from the Swiss National Science Foundation (SNSF) through project grant 200020_207349.

Some of the data presented in this Letter were obtained from the Mikulski Archive for Space Telescopes (MAST) at the Space Telescope Science Institute. The specific observations analyzed can be accessed via DOI:10.17909/wfg1-bm67 DOI:10.17909/je9x-d314.

Appendix
Fitting Codes Used to Analyze Cerberus's Spectral Energy Distribution

In this appendix, we give details of the codes used to analyze the SED of Cerberus and obtain its possible redshifts if it were an extragalactic object, as well as the implications of those redshifts in its physical properties.

We first used the EAZY code (Brammer et al. 2008) to fit the data in two ways: one using actual (low-S/N) flux measurements for all filters, and another replacing all S/N < 3 measurements by 5σ upper limits that templates were not allowed to surpass (achieved with a modified version of the code). We employed in the fits all v1.3 templates for stellar-dominated galaxies,[23] which include a dusty galaxy with a high equivalent width emission-line spectrum. We also allowed combinations of stellar-only templates with the new models for LRDs and high-redshift AGN+torus recently added based on JWST data (Killi et al. 2023). We did not impose any prior and

[23] As listed here: https://github.com/gbrammer/eazy-photoz/tree/master/templates.

worked with minimum χ^2 photometric redshift estimates in the range $0 < z < 20$.

We also ran BAGPIPES (Carnall et al. 2018). BAGPIPES is a stellar population synthesis modeling package built on the updated Bruzual & Charlot (2003) spectral library with the 2016 version of the MILES library (Falcón-Barroso et al. 2011). It uses a Kroupa (2001) IMF. We adopted a Calzetti et al. (2000) dust attenuation allowing 0 mag $< A_V <$ 8 mag and included nebular emission lines. The star formation history (SFH) is set to a delayed-τ model, and the code included an AGN component as in Carnall et al. (2023).

We fitted the extracted photometry of Cerberus with PROSPECTOR (Johnson et al. 2021) to constrain its photometric redshift and stellar population properties. We adopted the PROSPECTOR setup described in detail in Langeroodi et al. (2023) and Langeroodi & Hjorth (2023b). In brief, the SFH is modeled nonparametrically in five temporal bins with a continuity prior (see, e.g., Leja et al. 2019); nebular emission is added from the CLOUDY (Chatzikos et al. 2023) runs compiled in Byler et al. (2017); we treat the nebular and stellar metallicity as independent free parameters; and dust attenuation is modeled with a two-component model, one for the entire galaxy and one for the star-forming regions (Kriek & Conroy 2013). In a first PROSPECTOR run, redshift is fitted as a free parameter with a flat prior in $0 < z < 20$. We then reran the same PROSPECTOR setup, fixing the redshift to the best-fit values mutually agreed on using results from all the SED-fitting codes used in this work (see below).

Complementarily, we made use of LEPHARE++, the C++ latest evolution of the SED-fitting code LEPHARE (Arnouts et al. 2002; Ilbert et al. 2006) to fit the Cerberus photometry, following the approach of Moutard et al. (2024, in preparation). In brief, we considered stellar population synthesis models from Bruzual & Charlot (2003) with a Chabrier (2003) IMF and two metallicities ($Z_\odot$, 0.5 $Z_\odot$), assuming exponential SFHs with 0.1 Gyr $\leqslant \tau \leqslant$ 30 Gyr and delayed SFHs peaking after 1 and 3 Gyr. To take into account the strong contribution from the nebular emission lines that can occur at very young ages, they are added following the line ratios adopted by Saito et al. (2020), and their normalization is allowed to vary by a factor of four. Aiming to take into account extremely dusty galaxies, attenuation is considered through the laws of Calzetti et al. (2000) and Arnouts et al. (2013), with 0 mag $\leqslant E(B-V) \leqslant$ 1.5 mag, and dust IR reemission is taken into account following Béthermin et al. (2012). We finally ran LEPHARE++ on a grid between redshift $z = 0$ and 20.

Apart from the previous codes, which were used to both constrain a photometric redshift and determine the physical properties of Cerberus, we also performed SED modeling with SYNTHESIZER-AGN and CIGALE, first fixing the redshift (to several values; see below).

The SYNTHESIZER-AGN code assumes that the SED can be modeled with a composite stellar population (Pérez-González et al. 2003, 2008) and AGN emission coming from the accretion disk and the dust torus (Pérez-González et al. 2024). The stellar emission includes a young and a more evolved star formation event, each one described by a delayed exponential function with timescales between 1 Myr and 1 Gyr, and with ages from 1 Myr up to the age of the Universe at the redshift of the source. The attenuations of the emission from each stellar population are independent and described by a Calzetti et al. (2000) law, with A_V values ranging from 0 to 10 mag for each population. The stellar emission is described by the Bruzual & Charlot (2003) models, assuming a Chabrier (2003) IMF with stellar mass limits between 0.1 and 100 $M_\odot$, and the nebular emission is also considered (Pérez-González et al. 2003). The AGN emission is modeled with a QSO average spectrum (Vanden Berk et al. 2001; Glikman et al. 2006). The dust emission from the AGN is modeled with the self-consistent templates of AGN tori presented in Siebenmorgen et al. (2015), and dust emission linked to star formation is added using the models from Draine & Li (2007).

The CIGALE (Boquien et al. 2019) SED-fitting analysis assumes an SFH modeled using a constant star formation rate with ages ranging from 1 to 100 Myr. We adopted the stellar population models from Bruzual & Charlot (2003) with solar metallicity and the Chabrier (2003) IMF. We included nebular continuum and emission lines using solar metallicity, electron density of 100 cm^{-3}, and an ionized parameter equal to $\log(U) = -2$. The dust attenuation and far-IR emission use the Calzetti law (Calzetti et al. 2000) and the Draine et al. (2014) models, respectively. AGN emission is added using the Fritz et al. (2006) models following the initial parameters suggested by Ciesla et al. (2015).

The obtained photometric redshifts solutions are $z \sim 0.4$ (provided by PROSPECTOR and LEPHARE++), $z \sim 4$ (very prominent solution for EAZY, also detected weakly by PROSPECTOR and LEPHARE++), $z = 14$–15 (obtained by all codes), $z \sim 17$ (obtained by LEPHARE++), and $z \sim 19$ (obtained by BAGPIPES and LEPHARE++). We note that the $z \sim 0.4$ solution corresponds to a PAH line entering the F1000W passband, the $z \sim 4$ solution would imply Paα covered by the filter, for $z \sim 15$ Hα would contribute to the MIRI F1000W flux, and $z \sim 19$ means that the F1000W emission could be enhanced by Hβ and/or [O III] $\lambda\lambda$4960, 5008 emission.

We fitted the SED shown in Figure 4, which includes all flux data points with S/N > 3 and upper limits for the rest of the bands, using the codes described above. We checked that our results concerning the photometric redshift and physical properties (for the two parameters mentioned in the main text, the stellar mass and the dust attenuation) do not change significantly if we only use S/N > 5 fluxes and upper limits, or just S/N > 5 fluxes. More specifically, the photometric redshift solutions are the same, but with different statistical weights (i.e., the peaks vary their relative strength). Concerning the physical properties, variations were very similar to the systematic differences between the distinct estimations for the two properties that are consistent among all codes and techniques, given that they are constrained by the two robust observational properties of Cerberus, i.e., the low luminosity and red color. More specifically, for the stellar mass we obtained variations of 0.3 dex when using higher-S/N data for $z \sim 4$ and $z \sim 15$, and 0.7 dex for $z \sim 0.4$. For the dust content, we obtained differences of <0.3 mag in all cases, always remaining relatively high, above 3 mag, or finding a similarly obscured torus model.

ORCID iDs

Pablo G. Pérez-González https://orcid.org/0000-0003-4528-5639
Pierluigi Rinaldi https://orcid.org/0000-0002-5104-8245
Karina I. Caputi https://orcid.org/0000-0001-8183-1460
Javier Álvarez-Márquez https://orcid.org/0000-0002-7093-1877

Marianna Annunziatella https://orcid.org/0000-0002-8053-8040
Danial Langeroodi https://orcid.org/0000-0001-5710-8395
Thibaud Moutard https://orcid.org/0000-0002-3305-9901
Leindert Boogaard https://orcid.org/0000-0002-3952-8588
Edoardo Iani https://orcid.org/0000-0001-8386-3546
Jens Melinder https://orcid.org/0000-0003-0470-8754
Luca Costantin https://orcid.org/0000-0001-6820-0015
Göran Östlin https://orcid.org/0000-0002-3005-1349
Luis Colina https://orcid.org/0000-0002-9090-4227
Thomas R. Greve https://orcid.org/0000-0002-2554-1837
Gillian Wright https://orcid.org/0000-0001-7416-7936
Almudena Alonso-Herrero https://orcid.org/0000-0001-6794-2519
Arjan Bik https://orcid.org/0000-0001-8068-0891
Sarah E. I. Bosman https://orcid.org/0000-0001-8582-7012
Alejandro Crespo Gómez https://orcid.org/0000-0003-2119-277X
Daniel Dicken https://orcid.org/0000-0003-0589-5969
Andreas Eckart https://orcid.org/0000-0001-6049-3132
Macarena García-Marín https://orcid.org/0000-0003-4801-0489
Steven Gillman https://orcid.org/0000-0001-9885-4589
Manuel Güdel https://orcid.org/0000-0001-9818-0588
Thomas Henning https://orcid.org/0000-0002-1493-300X
Jens Hjorth https://orcid.org/0000-0002-4571-2306
Iris Jermann https://orcid.org/0000-0002-2624-1641
Álvaro Labiano https://orcid.org/0000-0002-0690-8824
Romain A. Meyer https://orcid.org/0000-0001-5492-4522
Florian Peiβker https://orcid.org/0000-0002-9850-2708
John P. Pye https://orcid.org/0000-0002-0932-4330
Thomas P. Ray https://orcid.org/0000-0002-2110-1068
Tuomo Tikkanen https://orcid.org/0009-0003-6128-2347
Fabian Walter https://orcid.org/0000-0003-4793-7880
Paul P. van der Werf https://orcid.org/0000-0001-5434-5942

References

Alcalde Pampliega, B., Pérez-González, P. G., Barro, G., et al. 2019, ApJ, 876, 135
Álvarez-Márquez, J., Labiano, A., Guillard, P., et al. 2023, A&A, 672, A108
Arnouts, S., Le Floc'h, E., Chevallard, J., et al. 2013, A&A, 558, A67
Arnouts, S., Moscardini, L., Vanzella, E., et al. 2002, MNRAS, 329, 355
Bacon, R., Accardo, M., Adjali, L., et al. 2010, Proc. SPIE, 7735, 773508
Bacon, R., Brinchmann, J., Conseil, S., et al. 2023, A&A, 670, A4
Bacon, R., Conseil, S., Mary, D., et al. 2017, A&A, 608, A1
Bagley, M. B., Pirzkal, N., Finkelstein, S. L., et al. 2024, ApJL, 965, L6
Barro, G., Perez-Gonzalez, P. G., Kocevski, D. D., et al. 2024, ApJ, 963, 128
Barrufet, L., Oesch, P. A., Weibel, A., et al. 2023, MNRAS, 522, 449
Bertin, E., & Arnouts, S. 1996, A&AS, 117, 393
Best, W. M. J., Dupuy, T. J., Liu, M. C., Siverd, R. J., & Zhang, Z. 2020, The UltracoolSheet: Photometry, Astrometry, Spectroscopy, and Multiplicity for 3000+ Ultracool Dwarfs and Imaged Exoplanets, v1.0.1, Zenodo, doi:10.5281/zenodo.4570814
Béthermin, M., Daddi, E., Magdis, G., et al. 2012, ApJL, 757, L23
Blain, A. W., Smail, I., Ivison, R. J., Kneib, J. P., & Frayer, D. T. 2002, PhR, 369, 111
Boquien, M., Burgarella, D., Roehlly, Y., et al. 2019, A&A, 622, A103
Bouwens, R. J., Illingworth, G. D., Oesch, P. A., et al. 2011, ApJ, 737, 90
Brammer, G. B., van Dokkum, P. G., & Coppi, P. 2008, ApJ, 686, 1503
Bruzual, G., & Charlot, S. 2003, MNRAS, 344, 1000
Burgasser, A. J., Bezanson, R., Labbe, I., et al. 2024, ApJ, 962, 177
Burgasser, A. J., Gerasimov, R., Bezanson, R., et al. 2024, ApJ, 962, 177
Byler, N., Dalcanton, J. J., Conroy, C., & Johnson, B. D. 2017, ApJ, 840, 44
Calzetti, D., Armus, L., Bohlin, R. C., et al. 2000, ApJ, 533, 682
Caputi, K. I., Lagache, G., Yan, L., et al. 2007, ApJ, 660, 97
Carnall, A. C., McLure, R. J., Dunlop, J. S., & Davé, R. 2018, MNRAS, 480, 4379
Carnall, A. C., McLure, R. J., Dunlop, J. S., et al. 2023, Natur, 619, 716
Chabrier, G. 2003, PASP, 115, 763
Chapman, S. C., Blain, A. W., Smail, I., & Ivison, R. J. 2005, ApJ, 622, 772
Chatzikos, M., Bianchi, S., Camilloni, F., et al. 2023, RMxAA, 59, 327
Ciesla, L., Charmandaris, V., Georgakakis, A., et al. 2015, A&A, 576, A10
Decarli, R., Aravena, M., Boogaard, L., et al. 2020, ApJ, 902, 110
Decarli, R., Walter, F., Gónzalez-López, J., et al. 2019, ApJ, 882, 138
Dey, A., Soifer, B. T., Desai, V., et al. 2008, ApJ, 677, 943
Dicken, D., García Marín, M., Shivaei, I., et al. 2024, arXiv:2403.16686
Draine, B. T., & Li, A. 2007, ApJ, 657, 810
Draine, B. T., Aniano, G., Krause, O., et al. 2014, ApJ, 780, 172
Eisenstein, D. J., Johnson, B. D., Robertson, B., et al. 2023a, arXiv:2310.12340
Eisenstein, D. J., Willott, C., Alberts, S., et al. 2023b, arXiv:2306.02465
Elbaz, D., Cesarsky, C. J., Chanial, P., et al. 2002, A&A, 384, 848
Elston, R., Rieke, G. H., & Rieke, M. J. 1988, ApJL, 331, L77
Engelbracht, C. W., Gordon, K. D., Rieke, G. H., et al. 2005, ApJL, 628, L29
Falcón-Barroso, J., Sánchez-Blázquez, P., Vazdekis, A., et al. 2011, A&A, 532, A95
Franco, M., Elbaz, D., Béthermin, M., et al. 2018, A&A, 620, A152
Franx, M., Labbé, I., Rudnick, G., et al. 2003, ApJL, 587, L79
Fritz, J., Franceschini, A., & Hatziminaoglou, E. 2006, MNRAS, 366, 767
Furtak, L. J., Shuntov, M., Atek, H., et al. 2023, MNRAS, 519, 3064
Galametz, A., Grazian, A., Fontana, A., et al. 2013, ApJS, 206, 10
Gillman, S., Gullberg, B., Brammer, G., et al. 2023, A&A, 676, A26
Glikman, E., Helfand, D. J., & White, R. L. 2006, ApJ, 640, 579
González-López, J., Decarli, R., Pavesi, R., et al. 2019, ApJ, 882, 139
González-López, J., Novak, M., Decarli, R., et al. 2020, ApJ, 897, 91
Graham, J. R., & Dey, A. 1996, ApJ, 471, 720
Greene, J. E., Labbé, I., Goulding, A. D., et al. 2024, ApJ, 964, 39
Grogin, N. A., Kocevski, D. D., Faber, S. M., et al. 2011, ApJS, 197, 35
Hainline, K. N., Helton, J. M., Johnson, B. D., et al. 2024, ApJ, 964, 66
Hamann, F., Zakamska, N. L., Ross, N., et al. 2017, MNRAS, 464, 3431
Hughes, D. H., Serjeant, S., Dunlop, J., et al. 1998, Natur, 394, 241
Ilbert, O., Arnouts, S., McCracken, H. J., et al. 2006, A&A, 457, 841
Johnson, B. D., Leja, J., Conroy, C., & Speagle, J. S. 2021, ApJS, 254, 22
Karalidi, T., Marley, M., Fortney, J. J., et al. 2021, ApJ, 923, 269
Killi, M., Watson, D., Brammer, G., et al. 2023, arXiv:2312.03065
Kocevski, D. D., Onoue, M., Inayoshi, K., et al. 2023, ApJL, 954, L4
Koekemoer, A. M., Ellis, R. S., McLure, R. J., et al. 2013, ApJS, 209, 3
Koekemoer, A. M., Faber, S. M., Ferguson, H. C., et al. 2011, ApJS, 197, 36
Kokorev, V., Caputi, K. I., Greene, J. E., et al. 2024, ApJ, 968, 38
Kolb, J., Madec, P.-Y., Arsenault, R., et al. 2016, Proc. SPIE, 9909, 99092S
Kriek, M., & Conroy, C. 2013, ApJL, 775, L16
Kroupa, P. 2001, MNRAS, 322, 231
Labbé, I., Greene, J. E., Bezanson, R., et al. 2023a, arXiv:2306.07320
Labbé, I., van Dokkum, P., Nelson, E., et al. 2023b, Natur, 616, 266
Langeroodi, D., & Hjorth, J. 2023a, ApJL, 957, L27
Langeroodi, D., & Hjorth, J. 2023b, arXiv:2307.06336
Langeroodi, D., Hjorth, J., Chen, W., et al. 2023, ApJ, 957, 39
Le Floc'h, E., Papovich, C., Dole, H., et al. 2005, ApJ, 632, 169
Leggett, S. K., Tremblin, P., Phillips, M. W., et al. 2021, ApJ, 918, 11
Leja, J., Carnall, A. C., Johnson, B. D., Conroy, C., & Speagle, J. S. 2019, ApJ, 876, 3
Madau, P., & Dickinson, M. 2014, ARA&A, 52, 415
Madec, P. Y., Arsenault, R., Kuntschner, H., et al. 2018, Proc. SPIE, 10703, 1070302
Magnelli, B., Elbaz, D., Chary, R. R., et al. 2009, A&A, 496, 57
Maiolino, R., Scholtz, J., Curtis-Lake, E., et al. 2023, arXiv:2308.01230
Marley, M. S., Saumon, D., Visscher, C., et al. 2021, ApJ, 920, 85
Matthee, J., Naidu, R. P., Brammer, G., et al. 2024, ApJ, 963, 129
McCarthy, P. J. 2004, ARA&A, 42, 477
Meisner, A. M., Leggett, S. K., Logsdon, S. E., et al. 2023, AJ, 166, 57
Melinder, J., Östlin, G., Hayes, M., et al. 2023, ApJS, 266, 15
Meyer, R. A., Barrufet, L., Boogaard, L. A., et al. 2024, A&A, 681, L3
Naidu, R. P., Oesch, P. A., Setton, D. J., et al. 2022, arXiv:2208.02794
Narayanan, D., Dey, A., Hayward, C. C., et al. 2010, MNRAS, 407, 1701
Nelson, E. J., Suess, K. A., Bezanson, R., et al. 2023, ApJL, 948, L18
Oesch, P. A., Brammer, G., Naidu, R. P., et al. 2023, MNRAS, 525, 2864
Oesch, P. A., Brammer, G., van Dokkum, P. G., et al. 2016, ApJ, 819, 129
Oke, J. B., & Gunn, J. E. 1983, ApJ, 266, 713
Pacucci, F., & Loeb, A. 2024, ApJ, 964, 154
Pacucci, F., Nguyen, B., Carniani, S., Maiolino, R., & Fan, X. 2023, ApJL, 957, L3

Papovich, C., Cole, J. W., Yang, G., et al. 2023, ApJL, 949, L18
Pérez-González, P. G., Barro, G., Annunziatella, M., et al. 2023a, ApJL, 946, L16
Pérez-González, P. G., Barro, G., Rieke, G. H., et al. 2024, ApJ, 968, 4
Pérez-González, P. G., Costantin, L., Langeroodi, D., et al. 2023b, ApJL, 951, L1
Pérez-González, P. G., Gil de Paz, A., Zamorano, J., et al. 2003, MNRAS, 338, 508
Pérez-González, P. G., Rieke, G. H., Egami, E., et al. 2005, ApJ, 630, 82
Pérez-González, P. G., Rieke, G. H., Villar, V., et al. 2008, ApJ, 675, 234
Perrin, M. D., Sivaramakrishnan, A., Lajoie, C.-P., et al. 2014, Proc. SPIE, 9143, 91433X
Pozzetti, L., & Mannucci, F. 2000, MNRAS, 317, L17
Rieke, G. H., Wright, G. S., Böker, T., et al. 2015, PASP, 127, 584
Rieke, M. J., Robertson, B., Tacchella, S., et al. 2023, ApJS, 269, 16
Rinaldi, P., Caputi, K. I., Costantin, L., et al. 2023, ApJ, 952, 143
Saito, S., de la Torre, S., Ilbert, O., et al. 2020, MNRAS, 494, 199
Sanders, D. B., & Sanders, I. F. 1996, ARA&A, 34, 749
Siebenmorgen, R., Heymann, F., & Efstathiou, A. 2015, A&A, 583, A120
Simpson, J. M., Swinbank, A. M., Smail, I., et al. 2014, ApJ, 788, 125
Smit, R., Bouwens, R. J., Labbé, I., et al. 2014, ApJ, 784, 58
Steidel, C. C., Giavalisco, M., Pettini, M., Dickinson, M., & Adelberger, K. L. 1996, ApJL, 462, L17
Suárez, G., & Metchev, S. 2022, MNRAS, 513, 5701
Tacchella, S., Eisenstein, D. J., Hainline, K., et al. 2023, ApJ, 952, 74
Tremonti, C. A., Heckman, T. M., Kauffmann, G., et al. 2004, ApJ, 613, 898
Tsai, C.-W., Eisenhardt, P. R. M., Wu, J., et al. 2015, ApJ, 805, 90
Übler, H., Maiolino, R., Curtis-Lake, E., et al. 2023, A&A, 677, A145
Vanden Berk, D. E., Richards, G. T., Bauer, A., et al. 2001, AJ, 122, 549
Wang, T., Schreiber, C., Elbaz, D., et al. 2019, Natur, 572, 211
Williams, C. C., Alberts, S., Ji, Z., et al. 2024, ApJ, 968, 34
Williams, C. C., Tacchella, S., Maseda, M. V., et al. 2023, ApJS, 268, 64
Wilson, G., Huang, J. S., Pérez-González, P. G., et al. 2004, ApJS, 154, 107
Wright, G. S., Rieke, G. H., Glasse, A., et al. 2023, PASP, 135, 048003
Yan, H., Dickinson, M., Eisenhardt, P. R. M., et al. 2004, ApJ, 616, 63
Zavala, J. A., Buat, V., Casey, C. M., et al. 2023, ApJL, 943, L9